Optimal vortex formation in a self-propelled vehicle

Robert W. Whittlesey[1] **and John O. Dabiri**[1,2],†

[1]Graduate Aeronautical Laboratories, California Institute of Technology Pasadena, CA 91125, USA

[2]Bioengineering, California Institute of Technology Pasadena, CA 91125, USA

Previous studies have shown that the formation of coherent vortex rings in the near-wake of a self-propelled vehicle can increase propulsive efficiency compared with a steady jet wake. The present study utilizes a self-propelled vehicle to explore the dependence of propulsive efficiency on the vortex ring characteristics. The maximum propulsive efficiency was observed to occur when vortex rings were formed of the largest physical size, just before the leading vortex ring would pinch off from its trailing jet. These experiments demonstrate the importance of vortex ring pinch off in self-propelled vehicles, where coflow modifies the vortex dynamics.

Key words: biological fluid dynamics, propulsion, vortex dynamics

1. Introduction

The presence of coherent vortical structures in the near-wake of a jet, hereafter referred to as 'vortex-enhanced propulsion', has been studied extensively and shown to increase propulsive performance in self-propelled vehicles (Siekmann 1962; Weihs 1977; Müller *et al.* 2000*a*; Krueger 2001; Krueger & Gharib 2003, 2005; Finley & Mohseni 2004; Choutapalli 2007; Bartol *et al.* 2008; Krieg & Mohseni 2008, 2010, 2013; Moslemi 2010; Moslemi & Krueger 2010, 2011; Ruiz, Whittlesey & Dabiri 2011). Weihs (1977), using many assumptions, analytically predicted an increase of 50 % in the average thrust through the use of vortex-enhanced propulsion. Later experimental work by Krueger & Gharib (2005) measured increases of up to 90 % of the propulsive thrust by optimization of the vortex ring characteristics. Ruiz *et al.* (2011) extended the results from stationary nozzles to a self-propelled vehicle, showing that vortex-enhanced propulsion can yield up to a 50 % increase in the propulsive efficiency over a steady jet.

The vortices formed during vortex-enhanced propulsion can be characterized using the vortex formation time, $\hat{t}_{GRS}$, defined as

$$\hat{t}_{GRS} \equiv \frac{L}{D_0} = \frac{\overline{U_p} t_p}{D_0}, \qquad (1.1)$$

where L is the length of a fluid slug ejected from the nozzle, D_0 is the nozzle diameter, $\overline{U_p}$ is the average piston velocity and t_p is the discharge time, as defined in Gharib,

† Email address for correspondence: jodabiri@caltech.edu

Rambod & Shariff (1998). This definition is based on the use of a piston–cylinder apparatus for producing vortex rings in a quiescent tank. The hat on $\hat{t}_{GRS}$ denotes a non-dimensional quantity. The formation time, $\hat{t}_{GRS}$, can be thought of physically as the non-dimensional piston travel distance (L) or alternatively as the non-dimensional pulse duration (t_p). Gharib *et al.* (1998) demonstrated that vortex ring pinch off, a phenomenon where a forming vortex ring is kinematically separated from its trailing jet, occurs at a critical formation time $\hat{t}_{GRS} \approx 4$. Krueger & Gharib (2003) showed that for isolated vortex rings the pulse-averaged thrust normalized by the momentum flux is maximized at this critical formation time, known as the formation number F. Krueger, Dabiri & Gharib (2003, 2006) further showed that the formation number, F, can be reduced from its typical value of 4 when in the presence of coflow, such as that occurring in a self-propelled vehicle.

Ruiz *et al.* (2011) achieved significant increases in propulsive efficiency using vortex-enhanced propulsion, but did not explore the dependence of propulsive efficiency on vortex formation time. Moslemi & Krueger (2010, 2011) and Nichols & Krueger (2012) explored a range of formation time for their self-propelled vehicle, however only for relatively low Reynolds numbers (2×10^2–2×10^4, based on the vehicle length). The present work explores a range of vortex ring formation times at higher Reynolds number, relevant to larger autonomous and manned underwater vehicle propulsion, to better understand the dependence of propulsive efficiency on vortex ring formation.

The self-propelled vehicle used in these experiments utilized self-excited oscillations of a collapsible tube under external pressure to generate vortex rings. By varying the flow rate and external pressure, a wide range of vortex ring formation times encompassing the threshold for vortex ring pinch off could be studied. The vehicle operated in the Reynolds number range of $Re = 9 \times 10^4$–1×10^6, based on vehicle length. The wake of the vehicle was characterized using laser Doppler velocimetry (LDV) and dye visualization in order to quantify propulsive efficiency and wake vortex dynamics.

This paper is organized as follows. Section 2 describes the self-propelled vehicle and mechanism for generating vortices in its near-wake. The results of the experiments are presented in § 3, with a particular emphasis on the vortex ring formation characteristics and their effect on the measured vehicle efficiency. Finally, § 4 discusses the results.

2. Methods

2.1. *Passive vortex generator design and vehicle integration*

2.1.1. *Main vehicle*

For the self-propelled tests, a passive vortex generator (PVG) was designed and retrofitted to an existing autonomous underwater vehicle (AUV), as shown in figure 1. The propeller of the AUV drove the flow through the PVG, which used the self-excited oscillations of a collapsible tube to generate vortex rings. The AUV used in these experiments (Virginia Tech 475 AUV) had a hull diameter of 12 cm, a length of 1 m, and was capable of travelling at a nominal speed of 1.5 m s^{-1} (Petrich, Neu & Stilwell 2007; Gadre *et al.* 2008; Petrich 2009; Petrich & Stilwell 2010). An umbilical cable was used to supply the AUV with power and to send control commands to the motor. The power for the AUV system (and for other electrical sensors) was generated by a power supply (Agilent 6674A) set to output 13.0 V.
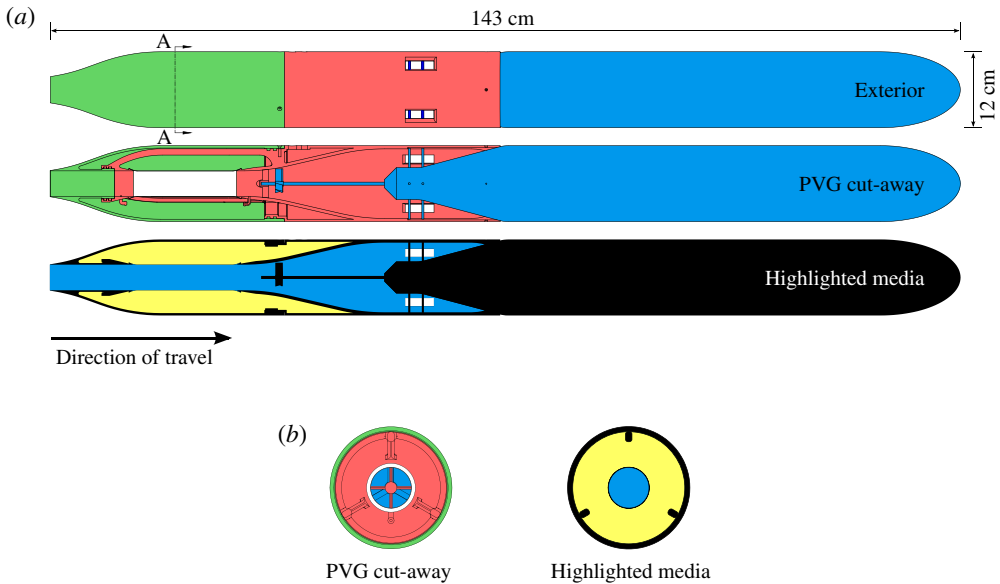
FIGURE 1. Schematic drawings of PVG-integrated AUV. (*a*) Side view of the PVG-integrated AUV. The top figure shows the complete system exterior with the centre figure showing the system with a cut plane parallel to the page through the middle of the PVG. The colours highlight the different components making up the assembly: blue is the AUV, red is the PVG internal frame, green is the PVG cover and white denotes the collapsible tube. The bottom figure highlights the different media within the device: blue is water, yellow is air and black is solid material. The section line, AA, in the top figure corresponds to the section view in (*b*). (*b*) Section view of the integrated PVG system (section line AA in *a*). The colouring in the left figure highlights the different components making up the assembly of the PVG and the right figure highlights the different media, as in (*a*).

The AUV components used in these experiments were based on standard remote-control hobby parts. A servo controller (Pololu Micro Maestro) was connected to the controlling computer. The servo controller commanded a motor speed controller (Hyperion Titan 20A Hi-Pro) attached to the AUV propeller motor (Hyperion ZS2209-30). This motor was geared down in a 40:19 ratio to the propeller shaft. The input to the motor, called the 'throttle setting' and hereafter denoted by T, was related to the pulse width for a servo control which was translated by the motor controller into a three-phase, pulse-width-modulated (PWM) signal for driving the motor. The throttle setting, T, ranged from 1000 (off) to 2000 (full throttle), with 1100 being the onset of motor rotation. The throttle setting values are related to the power delivered to the AUV motor.

The selection and optimal axial location of the propeller was determined iteratively. A variety of propellers were tested with varying pitch, diameter, and blade number. Maximal thrust was produced by a three-bladed, 47 mm diameter propeller with a pitch of 1.4 constructed of fibreglass-reinforced plastic. The propeller was mounted as far aft as possible without striking the sides of the PVG contraction (cf. figure 1).

2.1.2. *Integrated PVG design*

The PVG is composed of an elastic tube conveying fluid encased in an airtight box, schematically represented in figure 2. At certain values of the chamber pressure, P_e,
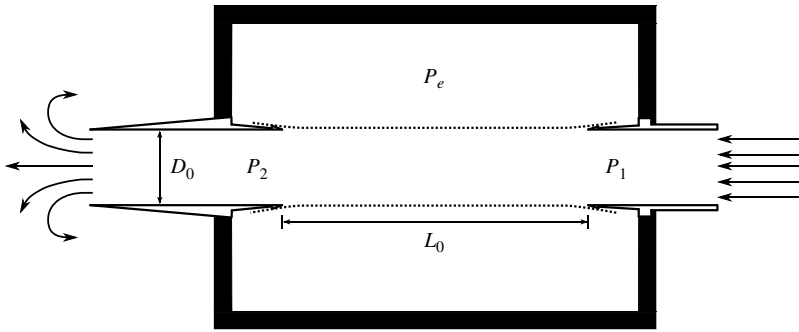
FIGURE 2. Schematic of a PVG. Flow enters the inlet from the right and exits into ambient fluid through the nozzle on the left. The collapsible tube is denoted in the dotted line and has length L_0 and diameter D_0. The pressure in the chamber is P_e, with the upstream and downstream pressures relative to the collapsible tube denoted by P_1 and P_2, respectively.

and flow rate through the tube, self-excited oscillations can be sustained which generate periodic pulses through the outlet (see Conrad 1969; Bertram 2003; Heil & Jensen 2003 and references therein). The pulses create vortex rings in the near-wake which enable a vehicle to use vortex-enhanced propulsion.

The design of the PVG upstream of the collapsible nozzle was adapted from the vehicle developed by Ruiz *et al.* (2011). The PVG-integrated AUV design is shown in figure 1(*a*). The PVG had a nozzle and tube diameter, D_0, of 4 cm and a collapsible tube length, L_0, of 16 cm. The wall thickness of the collapsible tube was 0.5 mm. The tube was constructed out of sheets of silicone with a Shore A durometer hardness of 35. The constructed tube had a glued seam, with an overlap of approximately 5 mm. The outer diameter of the PVG matched the diameter of the main vehicle to maximize the internal air chamber volume while minimizing form drag. In addition, the PVG added over 40 cm of length to the vehicle, making the total vehicle length 143 cm. The two-piece PVG was manufactured using stereolithography. This method yielded a smooth surface finish to minimize friction drag.

In order to reliably and accurately determine the oscillation frequency of the jet, the PVG was instrumented with a pressure transducer to measure the static pressure downstream of the collapsible tube (P_2 in figure 2). This pressure transducer measured the static pressure within the tube relative to the chamber pressure, P_e (cf. figure 2). This pressure is hereafter referred to as the 'transmural' pressure, $P_t = P_e - P_2$. The pressure tap was located 2 cm downstream of the collapsible tube (one-half of the tube diameter). The pressure transducer was attached to an instrumentation amplifier circuit and read by a data acquisition system (DAQ; figure 5, K). Because the pressure transducer was only used to measure frequency spectra (which was mean-subtracted), the pressure transducer and amplifier were calibrated using a water manometer for changes in pressure only. The DAQ system (National Instruments USB-6221) was connected to a computer (hereafter the DAQ computer) that accessed the DAQ system via the MATLAB (Mathworks) software program. The DAQ system was configured to record the pressure transducer signals at 5 kHz for the duration of a self-propelled run. This sampling rate was sufficiently high to capture the higher-order modes of the signal and to ensure that software-based post-filtering would remove noise within the signal. The highest frequencies recorded were noise in the 1–1.5 kHz range from the motor controller's PWM circuitry, thus the indicated sampling frequency of 5 kHz

satisfactorily encompassed the frequencies present within the laboratory environment. The DAQ system also recorded the voltage and current entering into the AUV vehicle. The current was measured by the voltage drop across a 0.05 Ω shunt resistor.

Ballast weight was added to the air chamber of the PVG to make the PVG approximately neutrally buoyant. The combination of the ballast weight and the pressure transducers yielded a PVG air chamber volume of 2600 ± 50 cm^3. For filling and draining the air in the chamber, two solenoid valves were used. One solenoid valve connected the PVG air chamber to a high-pressure line regulated at 75 kPa through a 0.25 mm diameter flow-control orifice and was used for filling the chamber, hereafter referred to as the fill solenoid valve. The other solenoid valve exhausted the PVG air chamber to the ambient, hereafter referred to as the exhaust solenoid valve. Both of these solenoid valves were controlled using a metal–oxide–semiconductor field-effect transistor (MOSFET)-based circuit that drove the high-current, 13 V solenoid using a low-current, 5 V digital signal from the DAQ board.

As the fill and exhaust solenoid valves were Boolean and not proportional, it was not feasible to precisely control the pressure in the chamber either manually or with a controller. Thus, the duration of time that the fill solenoid valve was open, hereafter referred to as the chamber fill time, τ, was used as an independent variable in the tests.

To observe the effect the chamber fill time, τ, has on the tube cross-sectional area, images of the tube along the axial direction were recorded at different values of τ. A sample of these images is shown in figure 3. Using these images, the area of the tube cross-sectional area was calculated and normalized by the area of the tube at $\tau = 0$ s to obtain a non-dimensionalized area fraction, α, defined as

$$\alpha \equiv \frac{A}{A_0}, \tag{2.1}$$

where A is the cross-sectional area of the tube and A_0 is the initial cross-sectional area of the tube (i.e. $\tau = 0$). These results are plotted in figure 4.

As shown in figure 3, it was observed that the tube undergoes buckling and collapse with a mode 3 azimuthal collapse. This is distinct from some earlier studies on collapsible tubes which showed a mode 2 azimuthal collapse (Conrad 1969; Kececioglu *et al.* 1981; Bertram & Nugent 2005; Bertram & Tscherry 2006; Bertram, Truong & Hall 2008). This is expected due to the relatively thin wall of the collapsible tube and the relatively short length of the tube used presently ($L_0/D_0 = 4$) (Love 1944; Palermo & Flaud 1987; Heil 1996; Fung 1997). It should be noted that the images shown in figure 3 are from conditions with no flow. However, during the self-excited oscillations, the tube was observed to maintain the same azimuthal mode number.

The mode 3 azimuthal collapse may contribute to a reduction in the sensitivity of α to τ due to the relationship between the tube compliance and its azimuthal collapse mode. Dion *et al.* (1995) showed that as the azimuthal mode of the tube buckling increased (e.g. from 2 to 3), the compliance of the tube decreased. A decreased compliance would yield a smaller change in the tube cross-sectional area for the same pressure change, and thus contribute to a sensitivity reduction.

2.2. *Test facility and cart system*

Experiments using the PVG-integrated AUV were conducted in a 40 m long free-surface water tunnel, a section of which is depicted in figure 5. The self-propelled tests
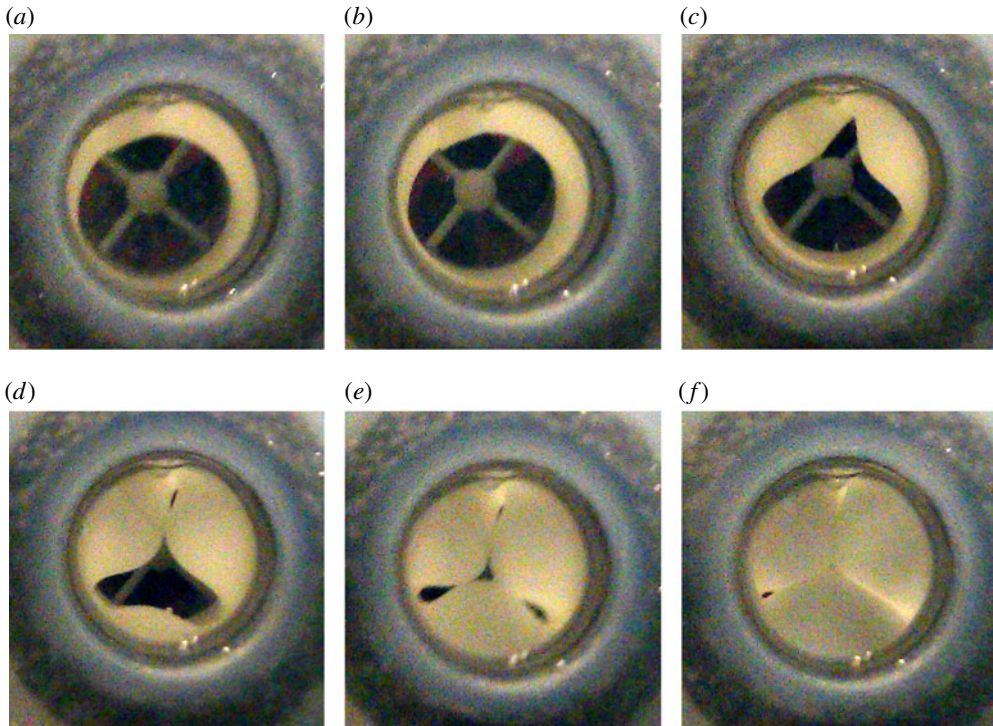
FIGURE 3. Axial view of tube collapse at different chamber fill times, τ, for the PVG with the propeller stationary. The collapsible tube is lightly coloured in these images with the PVG in grey. Images are aligned such that gravity points down: (*a*) $\tau = 0$ s; (*b*) $\tau = 4$ s; (*c*) $\tau = 8$ s; (*d*) $\tau = 12$ s; (*e*) $\tau = 15$ s; (*f*) $\tau = 20$ s.
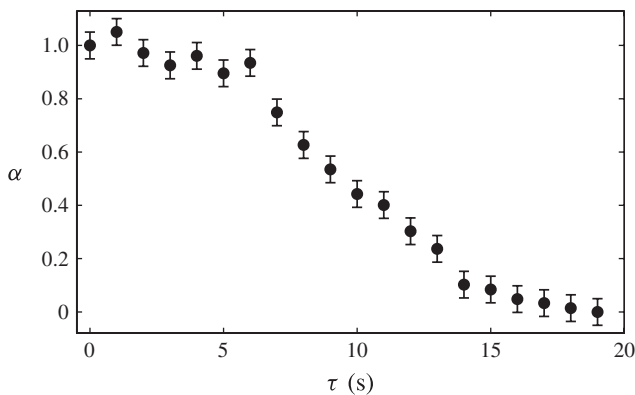

FIGURE 4. Cross-sectional area fraction of the collapsible tube from the PVG versus the chamber fill time, τ.

were conducted in a stationary ambient fluid. The AUV directly mounted to the slider of an air bearing (Nelson Air Corp, RAB6; figure 5, F) that restricted the motion of the AUV along the longitudinal direction of the test section to 10 cm of travel. The
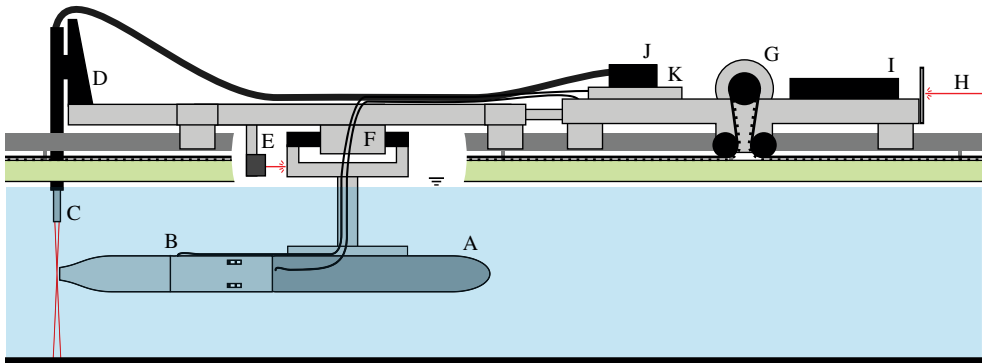
FIGURE 5. Schematic of a section of the facility used for the PVG-integrated AUV experiments. Letters indicate the item as follows: A, main vehicle (AUV); B, PVG; C, LDV probe for jet measurements; D, traverse for moving LDV probe; E, short-range laser distance sensor; F, air bearing carriage (slider in black); G, cart motor showing toothed belt and pulleys used to move cart; H, laser beam from long-range laser distance sensor; I, feedback controller box which interfaces to cart computer; J, LDV processing engine which receives back scattered light from LDV probe (C) and interfaces to DAQ computer; and K, DAQ system which interfaces to the DAQ computer.

carriage of the air bearing was mounted to a motorized cart system that moved on rails extending along the length of the tunnel test section. A feedback controller (figure 5, I) controlled the cart motor (figure 5, G) which moved the cart along the rails through the use of a toothed belt that extended the length of the tunnel. A short-range laser distance sensor (Micro-Epsilon, optoNCDT 1302; figure 5, E) rigidly mounted to the cart measured the distance to an optical target attached to the slider of the air bearing. The feedback controller measured the position of the AUV along the air bearing carriage using the short-range laser distance sensor and commanded the cart motor to move the cart such that the relative position of the AUV was kept at a reference value. In this way, the AUV was maintained within the 10 cm of air bearing travel while self-propelled along the full length of the water tunnel.

A long-range laser distance sensor (Micro-Epsilon, optoNCDT 1182; figure 5, H) measured the position of the cart along the tunnel. The combined values of the short- and long-range distance sensors precisely measured the position of the vehicle along the tunnel. The value of the position was Kalman filtered and used to obtain the position and velocity, U_∞, of the vehicle during self-propelled runs. An independent computer (hereafter the cart computer) sent control signals to the cart's feedback controller and recorded the cart's position and velocity. The cart computer was also responsible for issuing commands to the motor controller in the AUV.

2.3. *Procedure for self-propelled runs*

The throttle setting, T, and the chamber fill time, τ, were selected for each self-propelled run of the AUV. At the start of each run, the air chamber of the PVG was filled for the duration specified by τ. The self-propelled portion of the run was then initiated. After the self-propelled portion of the run was completed, the exhaust solenoid opened to allow the air chamber pressure to recover to the ambient lab pressure. The cart was then slowly towed to the starting position for the next run. After the cart reached its starting position, the system waited an additional 15 s to

ensure the air chamber pressure of the PVG, P_e, had completely recovered to ambient before ending the run.

The settling time of the tunnel between subsequent runs was evaluated to ensure that each run was initiated in sufficiently quiescent conditions. Tests were conducted at a variety of vehicle speeds and indicated no significant difference in results from sets of runs performed with no additional delay between runs versus sets of runs performed with a delay of the order of several minutes between runs. Thus, all subsequent runs were conducted without any systematic delay besides that required to initialize the next run.

2.4. *Laser Doppler velocimetry*

A laser Doppler velocimeter (figure 5, C) was used to measure the jet velocity in the near-wake, U_j. The laser Doppler velocimeter (LDV) system (Measurement Science Enterprise, Inc. miniLDV, one-component) used frequency shifting to obtain the fluid velocity along the axial direction of the jet. The probe was mounted to a two-axis traverse system (figure 5, D) that had 100 mm of travel in each direction lateral to the axial direction of the AUV. The traverse and the attached LDV probe were mounted directly to the AUV cart. As the AUV system was able to travel many centimetres along the air bearing, there was possible variability in the downstream distance of the probe volume from the PVG nozzle. However, recordings of the short-range laser distance sensor (measuring the relative position of the cart to the AUV) showed that the measurement volume was 0.23 ± 0.05 nozzle diameters (9.3 ± 2.0 mm, mean $\pm$ standard deviation) downstream of the PVG nozzle exit across all runs. The LDV system was controlled by a vendor-provided software program which controlled the traverse and data acquisition.

During self-excited oscillations, the tube cross-section could become non-uniform due to the collapse of the tube (cf. figure 3). To evaluate the influence of tube cross-section non-uniformity on the flow exiting the nozzle, two high-spatial-resolution profiles were taken of the jet exit. Each profile consisted of a grid of sampling locations spaced 5 mm apart. At each sampling location, 250 samples were taken and time-averaged to obtain the local flow velocity. As each self-propelled run generated a few tens of seconds of test time during which the submarine was steadily moving ($\partial U_\infty / \partial t \approx 0$), only a few locations could be sampled during each self-propelled run. Thus, for these tests the AUV was fixed in the tunnel while the recirculation pumps were turned on to create uniform ambient flow past the AUV. The two run conditions chosen for analysis were $\tau = 0$ and 10 s with $T = 1300$. Generally, these run conditions would result in a self-propelled AUV speed of 42 and 12 cm s^{-1}, respectively (cf. figure 10). Since the tests were aimed at evaluating the non-uniformity of the jet exit rather than reproducing jet exit velocities from the self-propelled cases the flow in the tunnel was set to approximately 20 cm s^{-1} to provide a nominally representative flow condition.

The results of the high-spatial-resolution LDV jet profiles are shown in figure 6. The spatial average of the time-averaged local velocities yielded mean jet speeds of 1.2 and 0.74 m s^{-1} for $\tau = 0$ and 10 s, respectively. The results show the expected non-uniformity in the jet, particularly for the $\tau = 10$ s case. The standard deviation of local time-averaged velocities across the exit was 5.4 and 13 % of the spatial average of the time-averaged local velocities for $\tau = 0$ and 10 s, respectively. Prior work has shown that small jets can emanate from the lobes of the collapsed tube during self-excited oscillations (Bertram *et al.* 2008; Truong & Bertram 2009). However, Bertram *et al.* (2008) found that these jets can dissipate quickly due to viscous
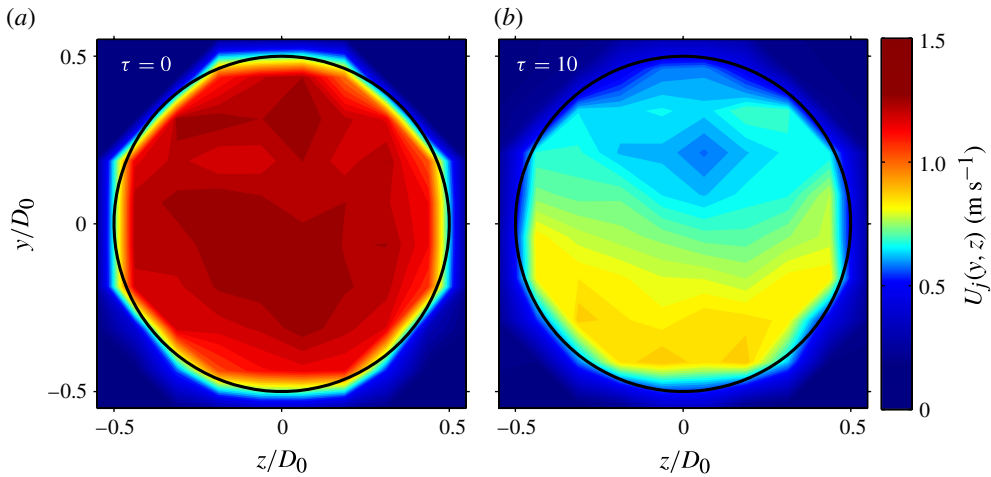
FIGURE 6. Contour plot showing the spatial variation in the mean local jet exit velocity for $T = 1300$ and $\tau = 0$ and 10 s. The left image is for $\tau = 0$ s and the right for $\tau = 10$ s. The colour indicates the magnitude of the local mean velocity in the x direction (aligned with the axial direction of the submarine). The lateral directions, y and z, are scaled by the diameter of the jet nozzle and the outline of the nozzle exit is shown as the white ring in each of the plots. The gravity vector is in the negative y direction.

diffusion (at low Reynolds number). Their absence from the results shown in figure 6 are likely due to turbulent dissipation within the jet. The non-uniformity observed in figure 6 is primarily due to the weight of the water within the collapsible tube altering the tube cross-section (cf. figure 3). Later measurements of the time-averaged jet velocity during self-propelled runs used the LDV probe volume centred on the nozzle and are assigned an additional conservative error of 13 % to account for the jet exit profile non-uniformity. The combined non-uniformity error was added to the traditional 95 % confidence interval using a root-mean-square (r.m.s.) method to obtain the total error for the jet velocity measurement. This enabled single runs to yield a complete set of measurements rather than necessitating data collection across several runs for each experimental condition (T, τ). It should be noted, however, that the centreline measurements inherently and systematically underestimate the spatially averaged jet exit velocity due to the observed spatial non-uniformity. The Froude propulsive efficiency calculated using the centreline data is therefore systematically overestimated (cf. (2.5)). Despite this limitation, trends in efficiency versus formation time can be clearly identified, as shown below.

2.5. *Dye visualization*

Dye visualizations of the vehicle wake were obtained by using a gravity-fed solution of slightly diluted food colouring injected into the inlet section of the PVG. A high-speed camera (Photron APS-RX) recorded video of the dyed wake at 125 Hz during self-propelled runs of the vehicle.

Example images from a representative test are shown in figure 7(*a*). To aid interpretation of the videos, the images of the wake were phase-averaged. The frequency of oscillation determined from the transmural pressure data, P_t, was used to select the images for averaging. Because the PVG-integrated AUV is in a different position in every image, each image was cross-correlated with a smaller cropped
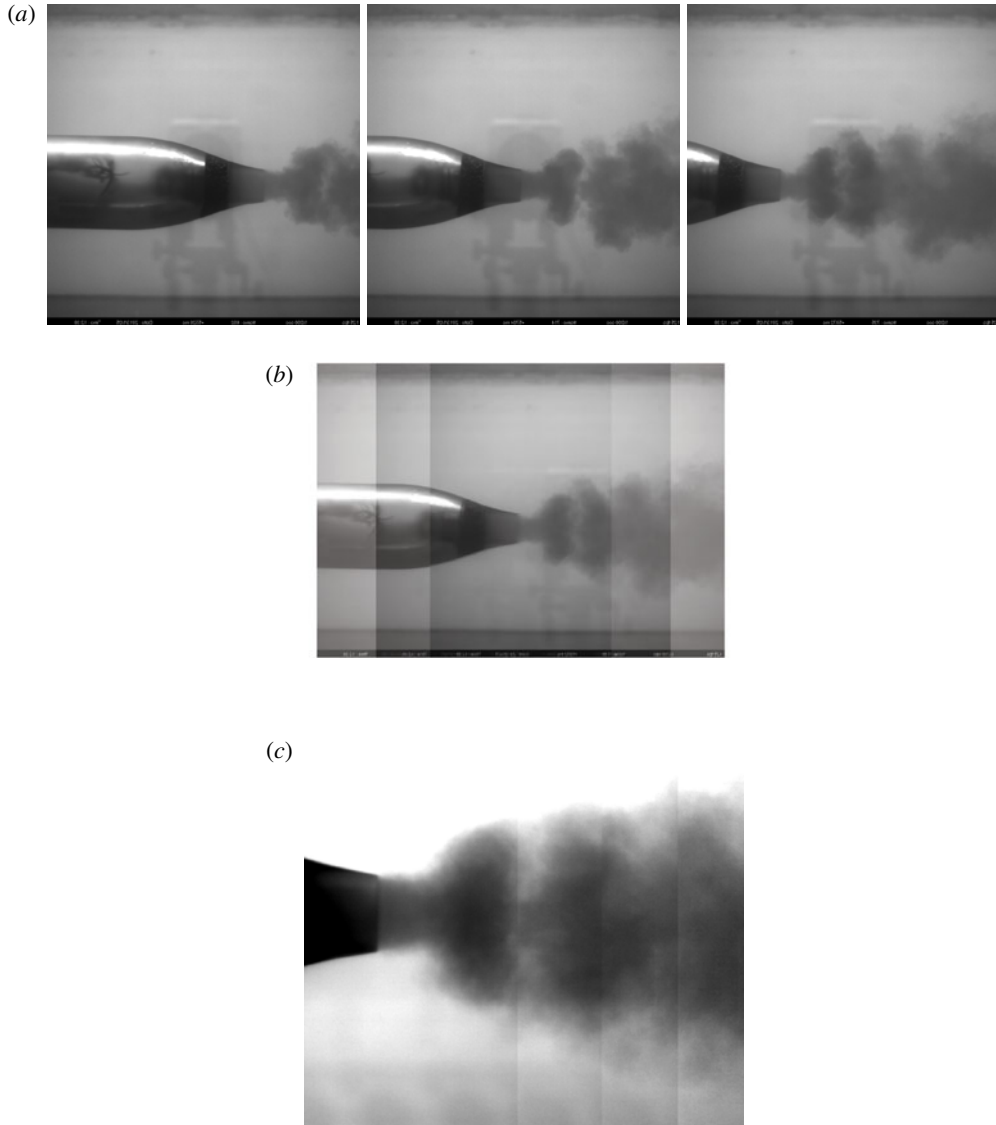
(*a*)

(*b*)

(*c*)

FIGURE 7. Example results from dye visualizations of PVG wake. (*a*) Example raw images from dye-visualization run with $T = 1700$ and $\tau = 10$. Each image is from approximately the same phase of the oscillation cycle and are approximately 0.16 s apart. (*b*) Simulated stacking of dye visualization images from (*a*). (*c*) Final phase-averaged result including images from (*a*) after stacking (demonstrated in *b*) and image correction (brightness and contrast). Vertical bars in the wake are a processing artefact due to moving image boundaries relative to PVG nozzle (cf. *b*). The phase-averaged frame consists of six frames averaged together.

image of the aft-most portion of the PVG nozzle. This allowed for accurate tracking of the vehicle in each image. Images that were integer periods apart were stacked and aligned by their cross-correlated nozzle exit positions, as demonstrated in figure 7(*b*). The stacked images were then summed in their pixel intensity values and divided by

the number of images stacked. Because each image that was added to the overall phase-averaged image covered a different extent of the domain (e.g. one image shows mostly PVG and little of the wake whereas another image shows mostly wake and little of the PVG), different regions of the phase-averaged images have different numbers of phases averaged (e.g. all images show the wake near the vehicle whereas fewer images show the wake far from the vehicle). The differing domain extent generates a visual artefact that is visible in the resulting phase-averaged dye images as faint vertical bars in the wake (see figure 7*c*).

2.6. *Formation time*

As discussed previously, the formation time of the ejected fluid characterizes the vortex rings that are produced (cf. § 1). The standard definition of formation time, $\hat{t}_{GRS}$, is given in (1.1). However, because the present system creates a train of vortex rings from a moving system, two modifications to the formation time definition were made.

The first adjustment follows from Krueger *et al.* (2003, 2006), who considered the creation of vortex rings created in coflow, where the ambient fluid is flowing parallel and in the same direction as the jetting fluid. They revised the formation time as

$$\hat{t}_{KDG} = \frac{t_p(\overline{U_p} + \overline{V_c})}{D_0},\tag{2.2}$$

where $\overline{V_c}$ is the average coflow velocity. This revised form of the formation time is appropriate for the current study as the self-propelled vehicle experiences ambient coflow in its frame of reference.

Because the ejection time $t_p \sim 1/f$, where f is the oscillation frequency, the second adjustment was to redefine the formation time for self-propelled pulsed jets as

$$\hat{t} = \frac{U_j + U_\infty}{fD_0},\tag{2.3}$$

where $\overline{U_p}$ and $\overline{V_c}$ have been replaced by U_j and U_∞, respectively, to match the current nomenclature. The oscillation frequency was calculated from the peak in the fast-Fourier transform of the mean-subtracted transmural pressure, P_t, during the steady-state portion of the self-propelled run. Furthermore, a threshold was applied to the amplitude of the peak of the Fourier-transformed P_t such that only runs with peak amplitudes exceeding this threshold were considered oscillating cases.

To assist in evaluating the existence of vortex ring pinch off, figure 8 shows both the planar laser-induced fluorescence (PLIF) image of vortex ring ejection for three formation times (from Gharib *et al.* 1998) and an illustrated silhouette depicting the expected image of the same event using room lighting and dark dye, as in the current experiments. For figure 8(*a,b*) where the formation time is less than the formation number ($\hat{t}/F < 1$), we expect to see the primary vortex ring along with a minimal amount of dye in its wake. In addition, as the formation number is increased, the size of the vortex ring created increases as well. However, for fluid ejections that are greater than the formation number ($\hat{t}/F > 1$), as seen in figure 8(*c*), bumps along the trailing jet form. These bumps correspond to secondary vortex rings that are created after the primary vortex ring has pinched off. The example in figure 8(*c*) is from a sufficiently high formation time ($\hat{t}/F = 2.0$) that many secondary rings have been created in the trailing jet.

Krueger *et al.* (2006) measured the formation number, F, at which a vortex ring pinches off from its trailing jet and found that F is dependent on the coflow conditions.
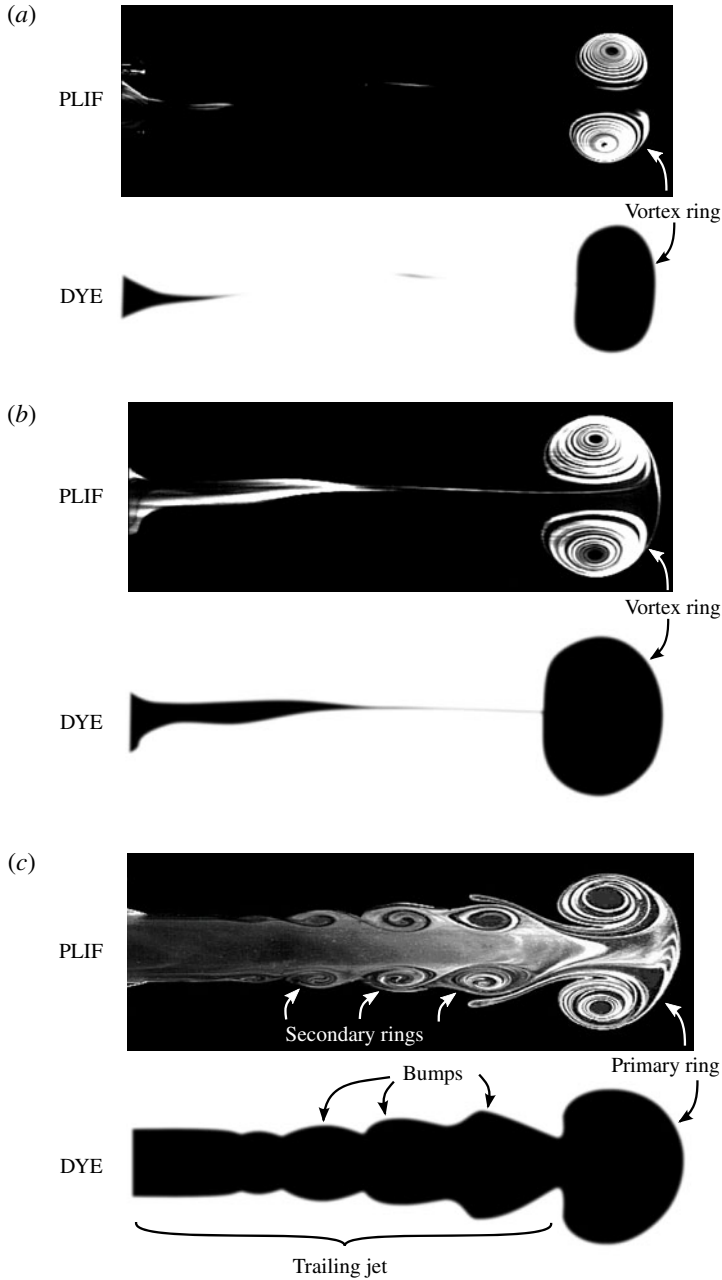
FIGURE 8. Top image in each panel is created using planar laser-induced fluorescence (PLIF) of a vortex ring ejection adapted from Gharib *et al.* (1998). The bottom image is a simulated dye visualization image (DYE) of the same event created using a silhouette of the PLIF image: (*a*) $\hat{t}/F = 0.5$; (*b*) $\hat{t}/F = 0.95$; (*c*) $\hat{t}/F = 2.0$.

They expressed the coflow conditions in terms of a velocity ratio, R_v, where

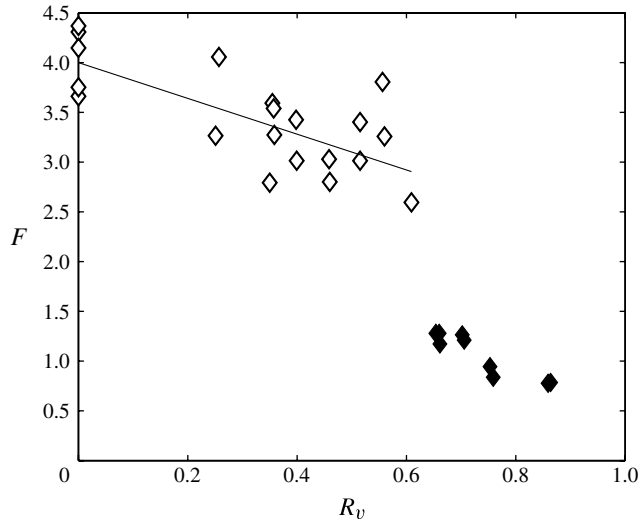$$R_v = \frac{U_\infty}{U_j}, \qquad (2.4)$$

FIGURE 9. Formation number, F, versus the velocity ratio, R_v, from Krueger *et al.* (2006). For velocity ratios less than 0.6, as indicated by the open markers, a linear fit of the data was obtained and is shown as the thin black line.
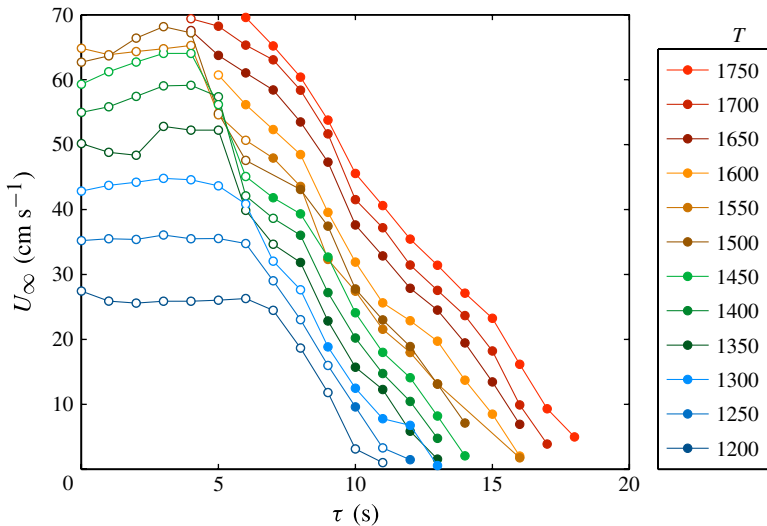

FIGURE 10. Vehicle velocity, U_∞, versus the chamber fill time for the throttle settings tested. Open symbols indicate non-oscillatory conditions (determined via thresholding of the FFT results of P_t) whereas closed symbols indicate oscillatory conditions. Error bars showing the bounds of a 95 % confidence interval are also plotted but are hidden by the marker size.

using the current nomenclature. Their results are replotted in figure 9. A significant feature in their results is the presence of a sharp transition in the formation number, F, around $R_v = 0.6$. Below the transition point shows a nearly linear trend and a least-squares fit was obtained (using the data points indicated with open markers in figure 9) to yield the equation $F \approx 4.0 - 1.8R_v$ ($0 \leqslant R_v \leqslant 0.6$, $r^2 = 0.52$).

2.7. *Efficiency*

The propulsive efficiency of the vehicle was calculated using the Froude efficiency, defined as

$$\eta \equiv \frac{2}{1 + \dfrac{U_j}{U_\infty}}, \tag{2.5}$$

where U_j is the time-averaged jet velocity and U_∞ is the time-averaged speed of the vehicle (Prandtl 1952). Although this definition is derived under the assumption of steady flow, it is applied presently as it provides an objective performance metric and is commonly used in propulsion studies. The application of this definition to unsteady flow conditions potentially constitutes a systematic error; therefore, its utility is limited to comparison among unsteady flow cases rather than with equivalent steady flows. This caveat should be noted when comparing the quantitative results of this paper with other work.

The present measurements were conducted using a single-component LDV probe. Therefore, radial and azimuthal components of velocity are not included in the efficiency measurement. Because these components leave additional kinetic energy in the wake without contributing to thrust, their neglect leads to overestimation of the actual propulsive efficiency.

2.8. *Error analysis*

For measurements that yield a Gaussian distribution, error bounds can be obtained through the use of Student's t distribution to obtain a 95 % confidence interval for the measurements (Beckwith, Marangoni & V, John 2007). For the jet velocity, U_j, the distribution of the sampled values is indeed Gaussian, even during oscillating regimes, owing to the significant level of turbulence in the jet. As such, the error bars for the mean jet velocity, U_j, are comprised of the 95 % confidence interval using Student's t distribution in addition to 13 % of the mean value, where the latter addition is due to the non-uniformity of the jet as observed in § 2.4. For any quantity that is calculated based on measured values, the error is propagated by summing the product of the error in the measured value and the sensitivity of the calculated quantity to that measured value in a root-mean squared fashion (Beckwith *et al.* 2007). To determine the measurement uncertainty of the oscillation frequency, the measured P_t during the steady portion of each run was divided into five equal time segments, and the oscillation frequency of each segment was determined by applying a fast Fourier transform (FFT) to the time-series data in each segment. The standard deviation of the frequencies in each of the five segments was then tabulated for every run to determine the measurement uncertainty of f, which was calculated to be nominally ± 1.0 Hz.

3. Results

3.1. *Vehicle speed*

The time-averaged vehicle speed, U_∞, is plotted in figure 10 for various values of T and τ. This yields a range of $Re = 90\,000$–$1\,000\,000$ based on the vehicle length. For $T = 1600$–1750, there is an absence of results for low chamber fill times because these runs were not self-propelled, as the cart reached maximum speed which saturated the controller output. For each throttle setting tested, the chamber fill time was increased until forward propulsion was no longer observed. The open symbols of figure 10
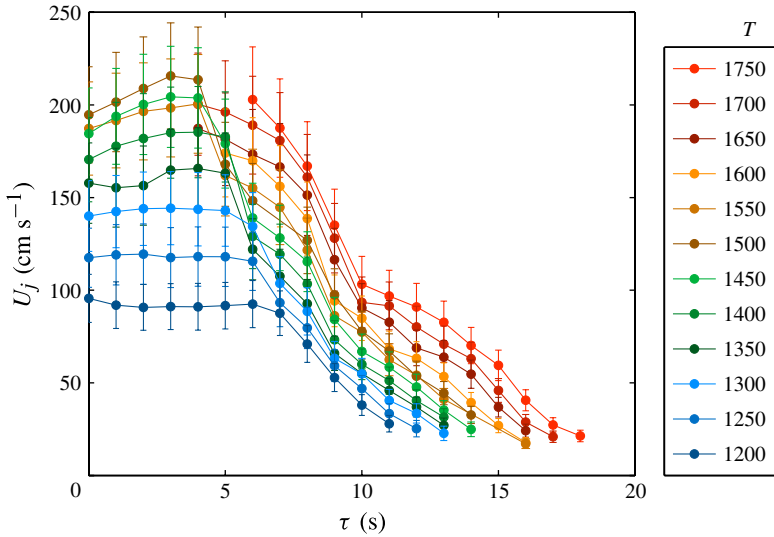
FIGURE 11. Averaged jet velocity, U_j, versus the chamber fill time for the throttle settings tested.

indicate steady jets whereas the closed symbols indicate self-excited oscillations within the jet, as determined by thresholding the P_t spectra.

In general, increasing T increases the vehicle speed. Furthermore, it is seen that there is a critical τ, τ_{crit}, after which the vehicle speed begins to decrease. The value of τ_{crit} decreases with increasing throttle setting and ranges from approximately 4 to 6 s at the high to low range of T, respectively. The value of τ_{crit} corresponds to the onset of significant tube cross-sectional area reduction as seen in figure 4. Thus, the plateau in U_∞ at low τ corresponds to the tube being in an uncollapsed state and acting as a straight tube.

3.2. *Jet velocity*

The measured average jet velocity, U_j, is plotted in figure 11. These results yield a jet Reynolds number, defined using the nozzle diameter and jet velocity, in the range of 7000–86 000, indicating that the jet was fully turbulent. The results mimic the general trends of the vehicle speed, shown in figure 10, where larger T yields higher velocities, and for $\tau > \tau_{crit}$, the jet velocity drops quickly with increasing τ. This is primarily related to the increasing flow resistance through the collapsible tube from decreasing tube cross-sectional area as τ is increased (cf. figure 4).

Figure 12 plots the phase-averaged jet velocity as a function of time. These plots are based on 50 oscillation periods that have been phase averaged and phase matched based on the trough of the oscillation period. From these figures, one can see that the jet velocity during an oscillation cycle can be generally described by a sinusoid of varying magnitudes. Furthermore, the jet velocity is nearly always greater than zero, with the exception of the brief axis-touching shown in figure 12(*e*). These plots are shown to give perspective on the jet pulse as a function of time, however, all future uses of U_j in equations and calculations simply use the time-averaged value and the uncertainty is calculated from the entire sampling domain without regard for phase.
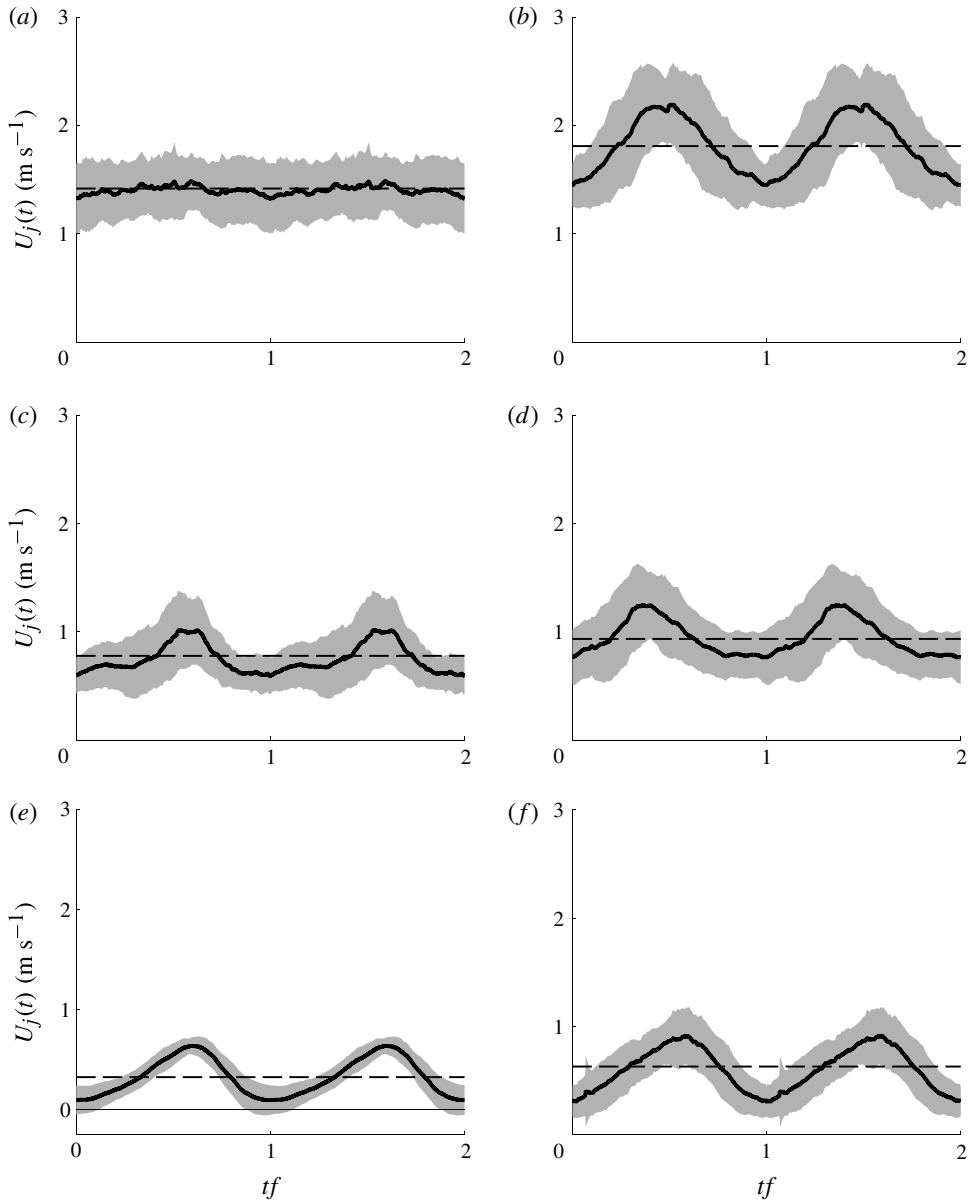
FIGURE 12. Phase-averaged measurements of the jet velocity at the centre of the jet. Each plot shows two phase-averaged oscillation cycles with time normalized by the oscillation period (the result is repeated for convenience). Each plot is generated from 50 oscillation periods averaged together with the phase-averaged velocity given by the thick black line and the standard deviation of the constitutive data denoted as the light grey banding. The thin dashed line is the overall time average from the entirety of LDV data for that self-propelled run: (a) $T = 1500$, $\tau = 7$ s; (b) $T = 1700$, $\tau = 7$ s; (c) $T = 1500$, $\tau = 10$ s; (d) $T = 1700$, $\tau = 10$ s; (e) $T = 1500$, $\tau = 14$ s; (f) $T = 1700$, $\tau = 14$ s.
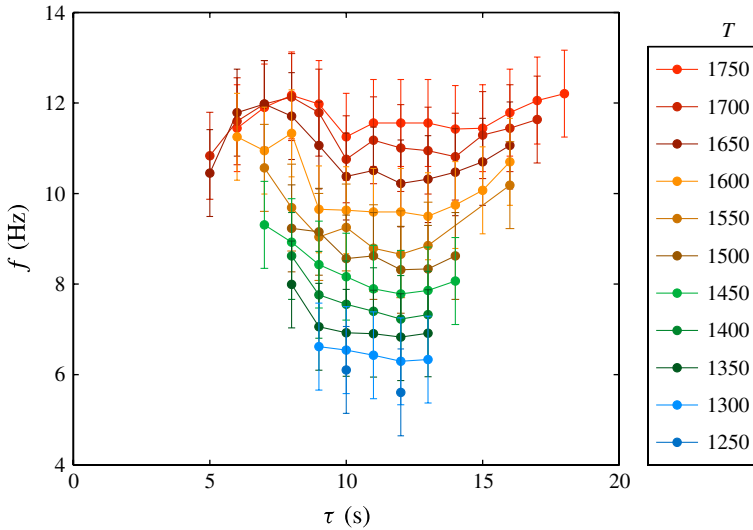
FIGURE 13. Oscillation frequency versus the chamber fill time for the variety of throttle settings tested. Error bars are plotted, however they are mostly obstructed by the markers.

3.3. *Oscillation frequency*

The oscillation frequency is plotted in figure 13. The value of f generally increases as T is increased. However, for a given value of T, there does not appear to be a strong relationship between f and τ, although a slight depression in f appears around $\tau = 10$–12 s.

3.4. *Efficiency*

Using the results for U_j and U_∞, the Froude efficiency, η, was calculated and is plotted in figure 14. In general, as T increases, η increases as well. For $\tau > 7$–8, where the tube has partially collapsed, the Froude efficiency, η, and its trend varies significantly depending on the throttle setting. For throttle settings 1300 and below, the Froude efficiency decreases sharply with increasing chamber fill time, τ. For throttle settings greater than 1300, the trends of the Froude efficiency appear to exhibit a well-defined maximum and then either decrease quickly or plateau briefly before dropping off. In all of these results, the sharp decreases are driven primarily by low U_∞ manifesting as low η (cf. figure 10).

The measured $R_v = U_\infty / U_j$ from the AUV system is plotted in figure 15. While the measured R_v varies, the maximum R_v is less than 0.6. Thus the linear fit obtained from the Krueger *et al.* (2006) can be used to obtain the coflow specific formation number, $F(R_v)$, under the assumption that the formation numbers measured by Krueger *et al.* (2006) apply to the PVG-generated vortex rings. It should be noted that the results obtained by Krueger *et al.* (2006) are from experiments where the jet flow and the coflow are initiated simultaneously whereas the current experiments have constant coflow with the jet flow modulated as function of time. While the experimental conditions were not identical, these results are used in lieu of conducting similar experiments as the difference is expected to be minimal because the jet flow typically does not reduce to zero between pulses in the current work (cf. figure 12) thus the initiating jet would not be disrupted by a strong wake from the vehicle motion.
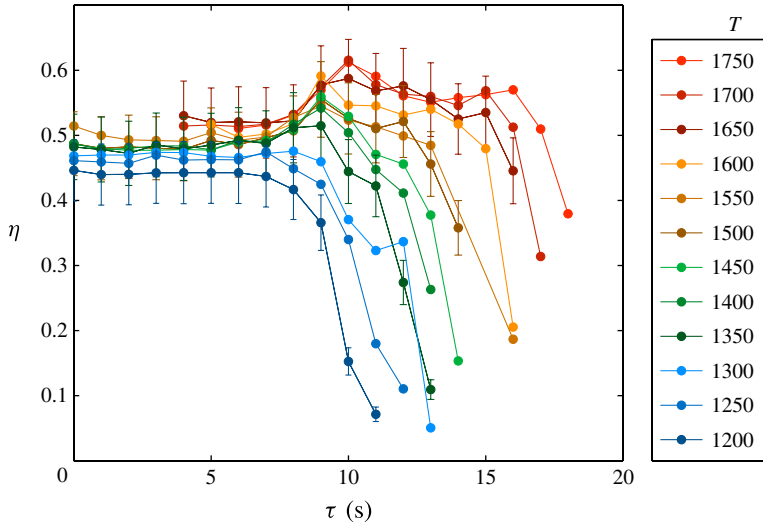
FIGURE 14. Froude efficiency, η, versus the chamber fill time for the throttle settings tested. Owing to excessive plot clutter, only a portion of the error bars have been plotted.
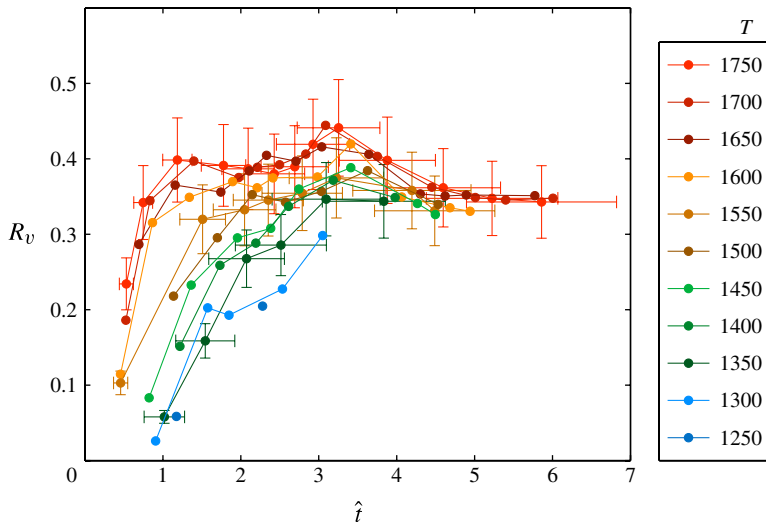

FIGURE 15. Velocity ratio, R_v, versus the coflow formation time, $\hat{t}$, for the throttle settings tested. Owing to excessive plot clutter, only a portion of the error bars have been plotted.

Equation (2.3) was used to calculate the formation time which was normalized by the coflow specific formation number, $F(R_v)$, to replot the efficiency values from figure 14. The normalized formation time plot is shown in figure 16. By plotting the data in this way, the peaks that were previously spread out in figure 14 have become aligned around $\hat{t}/F \approx 1$. Furthermore, the plot has flipped along the vertical direction as low values of η are correlated with low values of $\hat{t}/F$. This means that for low
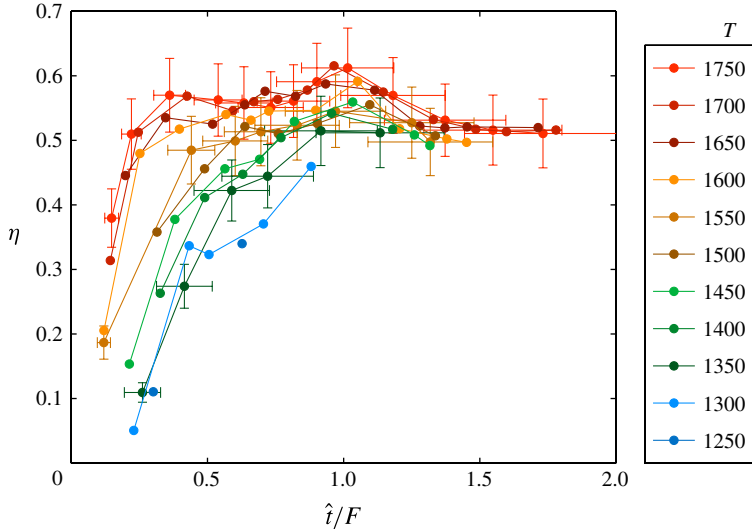
FIGURE 16. Froude efficiency versus the normalized formation time for the throttle settings tested. Owing to excessive plot clutter, only a portion of the error bars have been plotted.

formation times ($\hat{t}/F < 0.5$) the Froude efficiency η decreases rapidly with decreasing $\hat{t}/F$. The trend in η for $\hat{t}/F > 1$ appears to level off and plateau.

3.5. *Vortex ring formation*

Figure 16 highlights the observation that the peak in the Froude efficiency, η, corresponds to vortex ring pinch off where $\hat{t}/F = 1$. To demonstrate that this is indeed the case, it is illustrative to visualize the vortex ring formation at formation times below, at and above the formation number where $\hat{t}/F < 1$, $\hat{t}/F \approx 1$ and $\hat{t}/F > 1$, respectively.

With figure 8 in mind, let us consider the phase-averaged frames from the dye visualization at the end of the pulsation cycle. These are arranged in figure 17 according to their normalized formation time. Key differences exist between the single vortex ring images of figure 8 and the phase-averaged frames of figure 17. The first is that the results from the phase-averaged frames are from a series of vortex ring ejections, which create a train of vortex rings and yields much darker images. Second, the images from figure 8 were taken after the vortex ring had advected many diameters away from the vortex-generating nozzle. This yields a relatively thin amount of trailing dye for figure 8(*a,b*). This is in contrast to the images from the phase-averaged frames presented in figure 17 where the most recent primary vortex ring ejected is only a nozzle diameter away from the nozzle (or less). Because of this, the trailing dye is more significant in figure 17 than that shown in the example images of figure 8. However, as mentioned in § 2.6, the presence of a bump along the trailing jet is the criterion for determining if a vortex ring has pinched off.

For the images in figure 17, the number of phases averaged ranged from 4 to 16. This may be considered a low number for averaging, however the number of images was limited by vehicle speed and oscillation frequency. Also as noted previously (cf. § 2.5), within each image the downstream region contained fewer number of phases due to the moving domain of the constituent images. This is not a significant concern
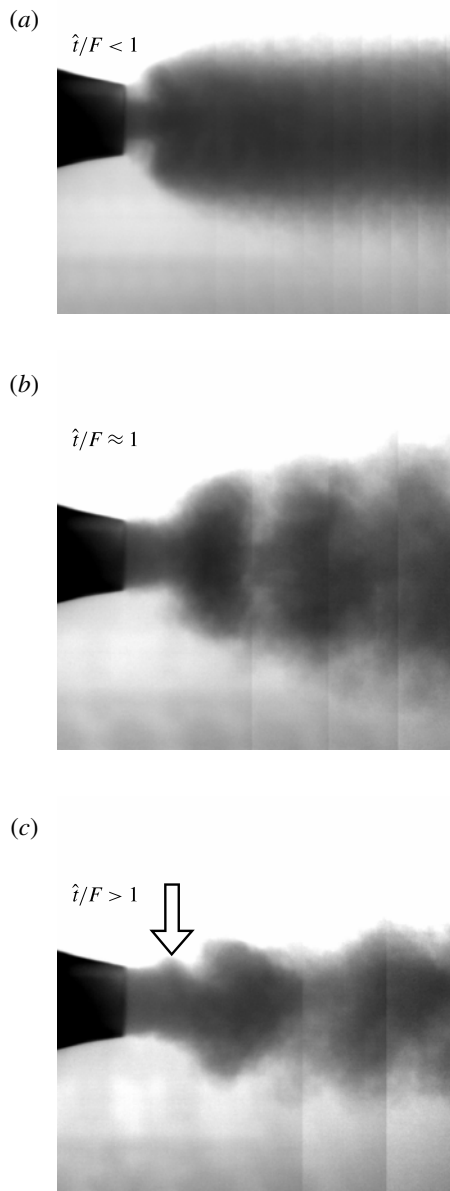
FIGURE 17. Phase-averaged dye visualizations images at the end of the pulsation cycle: (*a*) $\hat{t}/F = 0.24$, $T = 1700$ and $\tau = 16$ s (phase-averaged image consists of 14 images averaged); (*b*) $\hat{t}/F = 0.96$, $T = 1700$ and $\tau = 10$ s (phase-averaged image consists of 6 images averaged); (*c*) $\hat{t}/F = 1.48$, $T = 1700$ and $\tau = 7$ s (phase-averaged image consists of 4 images averaged). The arrow indicates the location of a bump in the trailing jet.

as the area of interest for determining vortex ring pinch off is isolated to the region closest to the nozzle, which contains the highest number of averaged phases.

A phase-averaged dye visualization for a run with a low value of the normalized vortex formation time, $\hat{t}/F < 1$, is shown in figure 17(a) with a normalized formation time of $\hat{t}/F = 0.24$. The train of dyed vortex rings in this image makes the individual vortex rings more difficult to discern; however comparison with the other images of figure 17 shows that the conditions in (a) yield the smallest vortex rings in both diameter and axial extent (compared with their higher-τ counterparts for the same T) with the least amount of trailing dye, both of which are consistent with a low-formation-time vortex ring.

A phase-averaged dye visualization for a run with the vortex formation time near the formation number, where $\hat{t}/F \approx 1$, is shown in figure 17(b). This dye visualization image depicts vortex rings that appear to be larger in size than in figure 17(a), as expected. The amount of trailing dye in figure 17(b) is much greater than figure 8(b) suggests it should be, however, as mentioned previously, this is likely a consequence of the image being recorded when the vortex ring is close to the nozzle rather than advected further downstream (as in figure 8). Furthermore, the trailing dye shows no bumps indicating the vortex ring has not pinched off from the trailing jet.

Finally, the case of a formation time greater than the formation number, where $\hat{t}/F > 1$, is shown in figure 17(c). While the primary vortex ring in figure 17(c) is not as coherent as in the other images of figure 17, a bump trailing behind the primary ring is visible in the image as indicated by the arrow. In contrast to figure 8(c), figure 17(c) shows only one secondary vortex ring (one bump) is created, but that is consistent with the lower normalized formation time of figure 17(c) ($\hat{t}/F = 1.48$ versus 2.0 of figure 8c). It should be noted that this bump is not a single random occurrence, but in fact is present in each pulse as this image is obtained from several frames phase-averaged together. This indicates that the primary vortex ring has indeed pinched off from the trailing jet.

It should be noted that there are instances in the literature where the leading secondary vortex ring from the trailing jet can be entrained further downstream into the primary ring (Gharib *et al.* 1998). However, this was not observed in our dye visualization studies. In addition, the bump criterion is only useful for conditions sufficiently greater than $\hat{t}/F = 1$ and can only reliably show the presence of secondary vortices and not their absence. The dye method is not precise enough to accurately identify a bump under conditions closer to vortex ring pinch off but where vortex ring pinch off is expected to occur (e.g. $\hat{t}/F = 1.1$).

In addition, the conditions of figure 17(b) correspond to the same conditions that yielded the highest propulsive efficiency. This case, where $\hat{t}/F \approx 1$, also shows an increased rate of jet spreading that is indicative of higher entrainment (Ho & Gutmark 1987; Liepmann & Gharib 1992; Reynolds *et al.* 2003). Ruiz *et al.* (2011) similarly found that a pulsed jet exhibited increased entrainment over a steady jet for a self-propelled vehicle. This increased entrainment is also identified through the larger size of the primary vortex ring of figure 17(b) compared with figure 17(a,c).

4. Discussion and conclusions

The present results demonstrate that a peak in the efficiency of vortex-enhanced propulsion occurs under conditions for which vortex rings of maximum size are generated, just at the onset of vortex ring pinch off. The maximum efficiency was found at a normalized formation time near $\hat{t}/F \approx 1$ for all of the cases tested, and a
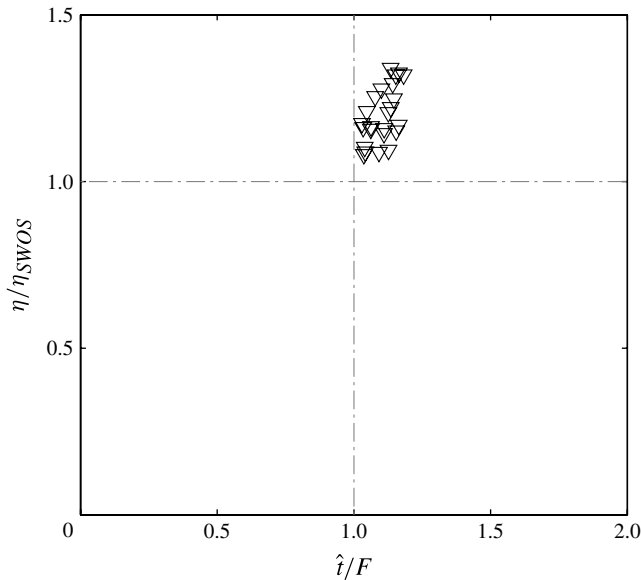
FIGURE 18. Data from Ruiz *et al.* (2011) has been replotted based on the normalized formation time so as to better match the presentation of the current results.

plateau in efficiency was observed for large values of $\hat{t}/F$. These results are consistent with previous work, as discussed below.

4.1. *Comparison with other results*

The observed peak in efficiency shown in figure 16 correlates well with the work of Krueger & Gharib (2003), who showed that the thrust normalized by the momentum flux is maximized at vortex ring pinch off ($\hat{t}/F = 1$). To compare against other self-propelled results, figure 18 shows a reanalysis of the results of Ruiz *et al.* (2011). In Ruiz *et al.* (2011), the control experiments used the vehicle operating with the rotating shell removed, a case denoted 'SWOS' for 'steady (jet) without shell'. Thus, the normalized efficiency is calculated as η/η_{SWOS} and is plotted against the normalized formation time (recalculated using (2.3) and the linear fit to the velocity ratio from Krueger *et al.* (2006)).

Comparison of figures 16 and 18 shows that despite the different mechanisms for generating vortex rings, the results of Ruiz *et al.* (2011) provide additional insight for the present work. In particular, the results of Ruiz *et al.* (2011) are primarily clustered around a normalized formation time of 1 and show an increase in the efficiency of the vehicle with vortex ring formation in its near-wake versus the same vehicle propelled by a steady jet. Although we are unable to make a similar quantitative comparison of the steady and unsteady jets in the current work, the results of Ruiz *et al.* (2011) suggest a similar advantage of pulsed jet propulsion near $\hat{t}/F = 1$ over steady jet propulsion in the present study.

Moslemi & Krueger (2010, 2011) and Nichols & Krueger (2012) studied self-propulsion using a vehicle called 'robosquid' which used a pulsation mechanism different from either Ruiz *et al.* (2011) or the current work. The results obtained using

the robosquid vehicle showed that decreasing formation time yielded a monotonic increase in the efficiency, in contrast with the present results. The discrepancy may be related to the different mechanism of vortex ring formation in robosquid that created a fully pulsed jet with greater enhancement of thrust. Krueger & Gharib (2003) showed that over-pressurization of the nozzle exit during vortex ring formation is one of the contributing factors to improving propulsive efficiency. It is likely that the robosquid vehicle, which uses a piston driven by a stepper motor to generate vortex rings, was able to generate significant nozzle exit over-pressure, even at low formation times, as the force generated by the accelerating flow was directly driven by a motor-driven piston. This is supported by the fact that the contribution of the nozzle exit over-pressure to the total impulse increases with decreasing formation time based on results from Krueger & Gharib (2003), who used a similar motor-driven piston mechanism. Thus, it is believed that the impulse from the nozzle exit over-pressure in the current PVG-based vehicle is less than that generated by the motor-driven piston of robosquid for low formation times. However, this theory cannot be confirmed by the current results as measurements of impulse generation during vortex ring ejection were not a part of the current study. It is also possible that differences in methods used to calculate propulsive efficiency may also have contributed to the observed discrepancies in the results. The robosquid efficiency results were obtained based on calculations of the wake kinetic energy and thrust from digital particle image velocimetry (DPIV) measurements. This is in contrast to the method used presently.

4.2. *Model predictions*

Ruiz *et al.* (2011) developed an analytical model for predicting the efficiency of a pulsed-jet vehicle. Under various assumptions such as $\hat{\imath}/F < 1$ and that the frequency of oscillations f is sufficiently high such that $\partial U_\infty/\partial t \approx 0$, the efficiency of the vehicle, η_{RWD}, can be expressed as

$$\eta_{RWD} \approx \frac{2}{3}(1 + \alpha_{xx})\frac{U_\infty}{U_j}, \qquad (4.1)$$

where α_{xx} is the added mass coefficient for the forming vortex ring accelerating in the axial direction of the flow. Using the dye visualizations of the vortex rings at the end of the pulsation cycle (cf. figure 17) the vortex bubble, defined as the volume of fluid that moves with the vortex ring (Maxworthy 1972), can be obtained. In general, the vortex bubble is obtained through streamline analysis (Shariff & Leonard 1992; Dabiri & Gharib 2004), dye visualization (Shariff & Leonard 1992) or, more recently, Lagrangian coherent structures (LCS) (Shadden, Dabiri & Marsden 2006). Olcay & Krueger (2008) measured the vortex bubble size using all three methods. They found that in all cases, the dye method underestimated the vortex volume after completion of vortex ring formation and that the error increased in time. The increasing error was due to the vortex bubble volume increasing through ambient-fluid entrainment and the diffusion of vorticity, both of which are not reflected in dye visualization results.

While it is known that the volume of the vortex bubble will be underpredicted by using the dye method, Olcay & Krueger (2008) show at the end of a pulsation cycle that this error is, at worst, 10 % of the total volume and thus we assume that this results in a 5 % error in each lateral dimension of the vortex ring.

Under the assumption that the vortex ring can be modelled as an oblate ellipsoid of revolution, the resulting vortex bubbles are approximated using ellipses as shown in figure 19. The ellipses were fit by eye based on the approximate location of the
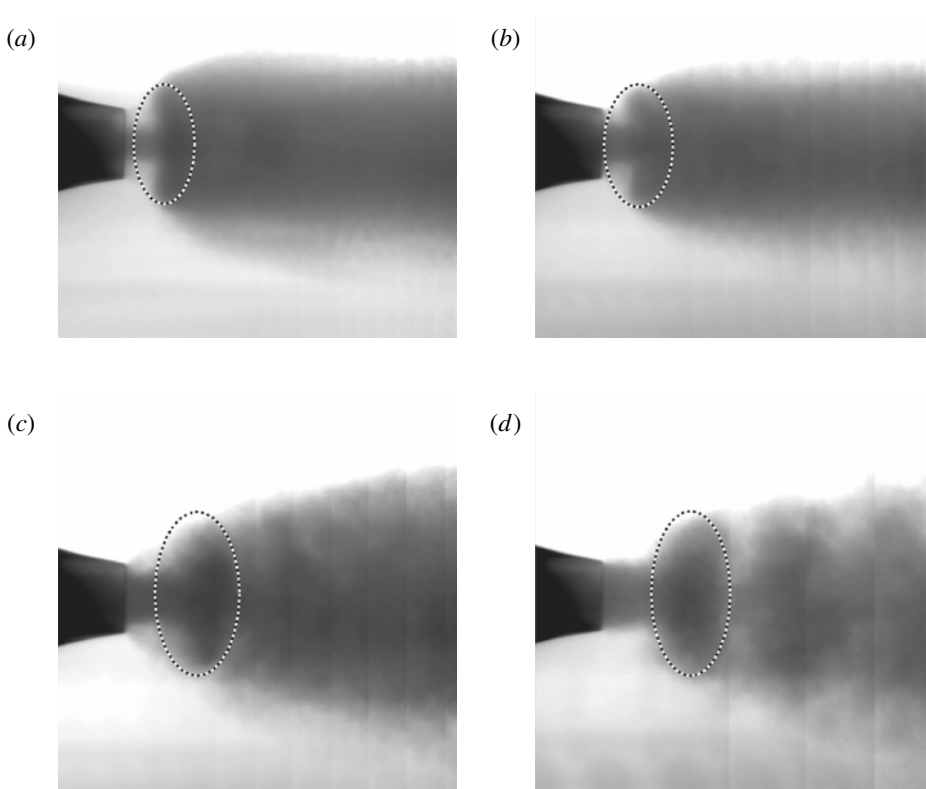
(*a*)

(*b*)

(*c*)

(*d*)

FIGURE 19. Ellipses were fit to the dyed vortex ring visible at the end of the pulsation cycle and represent the vortex bubble: (*a*) $\hat{t}/F = 0.31$, $T = 1500$ and $\tau = 14$ s, with $\alpha_{xx} = 1.09 \pm 0.06$; (*b*) $\hat{t}/F = 0.24$, $T = 1700$ and $\tau = 16$ s, with $\alpha_{xx} = 0.98 \pm 0.05$; (*c*) $\hat{t}/F = 0.89$, $T = 1500$ and $\tau = 10$ s, with $\alpha_{xx} = 1.08 \pm 0.06$; (*d*) $\hat{t}/F = 0.96$, $T = 1700$ and $\tau = 10$ s, with $\alpha_{xx} = 1.17 \pm 0.07$.

vortex cores in the images for the major axis and the streamwise extent of the darkest dye region for the minor axis, as the darkest dye was from the most recent ejection. From the major and minor axes of the fitted ellipse, an ellipsoid of revolution was constructed and used to calculate the added mass coefficient for the vortex bubble. The equation for the added mass coefficient of an ellipsoid (Green 1835) was evaluated numerically with the error bounds obtained by perturbing the lateral dimension 5 %. The calculated added mass coefficients ranged from 0.98 to 1.17 which reflect the significant oblateness of the vortex bubbles. Using (4.1), the pulsed jet efficiency was calculated and is compared to the standard Froude efficiency in figure 20. In general, one can see that the pulsed jet model yields results that are consistent with the Froude efficiency to within experimental error. Thus, for the present experiments one would expect to see a similar trend in the pulsed jet efficiency, η_{RWD}, with the maximum efficiency at $\hat{t}/F = 1$ as was found in the Froude efficiency results (e.g. figure 16).

The close agreement between η and η_{RWD} further supports the use of the Froude efficiency definition in the current work, as η_{RWD} was derived using assumptions of unsteadiness in the wake.
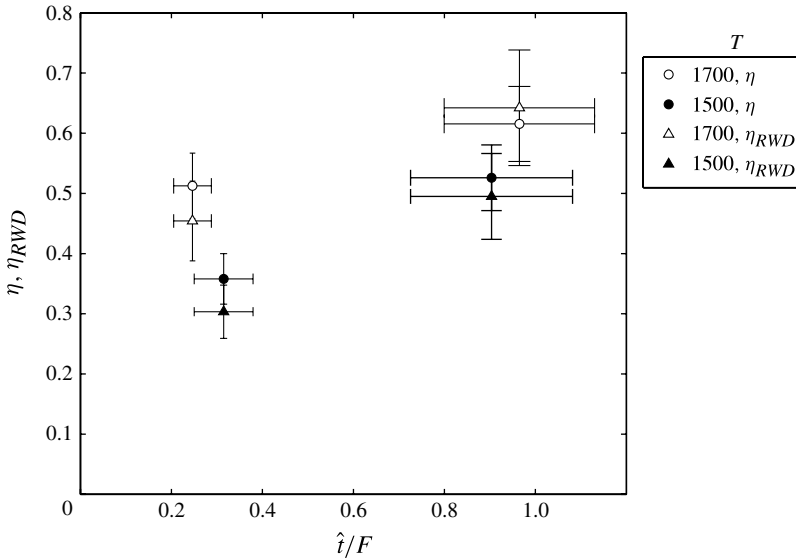
FIGURE 20. Pulsed jet efficiency, η_{RWD}, and the Froude efficiency, η, versus the normalized formation time, $\hat{t}/F$, for two values of T. The conditions plotted have their wake structures and vortex bubbles shown in figure 19.

Acknowledgements

REFERENCES

BARTOL, I. K., KRUEGER, P. S., THOMPSON, J. T. & STEWART, W. J. 2008 Swimming dynamics and propulsive efficiency of squids through ontogeny. *Integr. Compar. Biol.* **48** (6), 720–733.

BECKWITH, T. G., MARANGONI, R. D. & LIENHARD, J. H. 2007 *Mechanical Measurements*. Pearson Prentice Hall.

BERTRAM, C. D. 2003 Experimental studies of collapsible tubes. In *Flow Past Highly Compliant Boundaries and in Collapsible Tubes*, Fluid Mechanics and Its Applications, Vol. 72, pp. 51–65. Springer.

BERTRAM, C. D. & NUGENT, A. H. 2005 The flow field downstream of an oscillating collapsed tube. *Trans. ASME: J. Biomech. Engng* **127**, 39–45.

BERTRAM, C. D., TRUONG, N. K. & HALL, S. D. 2008 Piv measurement of the flow field just downstream of an oscillating collapsible tube. *Trans. ASME: J. Biomech. Engng* **130**, 061011.

BERTRAM, C. D. & TSCHERRY, J. 2006 The onset of flow-rate limitation and flow-induced oscillations in collapsible tubes. *J. Fluids Struct.* **22**, 1029–1045.

CHOUTAPALLI, I. M. 2007 An experimental study of a pulsed jet ejector. PhD thesis, Florida State University.

CONRAD, W. A. 1969 Pressure-flow relationships in collapsible tubes. *IEEE Trans. Biomed. Engng* **BME**-16 (4), 284–295.

DABIRI, J. O. & GHARIB, M. 2004 Fluid entrainment by isolated vortex rings. *J. Fluid Mech.* **511**, 311–331.

DION, B., NAILI, S., RENAUDEAUX, J. P. & RIBEAU, C. 1995 Buckling of elastic tubes: study of highly compliant device. *Med. Biol. Engng Comput.* **33**, 196–201.

FINLEY, T. J. & MOHSENI, K. 2004 Micro pulsatile jets for thrust optimization. In *Proceedings of IMECE2004, 2004 ASME International Mechanical Engineering Congress and Exposition*.

FUNG, Y. C. 1997 *Biomechanics: Circulation*. Springer.

GADRE, A. S., MACZKA, D. K., SPINELLO, D., MCCARTER, B. R., STILWELL, D. J., NEU, W., ROAN, M. J. & HENNAGE, J. B. 2008 Cooperative localization of an acoustic source using towed hydrophone arrays. In *Autonomous Underwater Vehicles, 2008 (AUV 2008)*, pp. 1–8. IEEE/OES.

GHARIB, M., RAMBOD, E. & SHARIFF, K. 1998 A universal time scale for vortex ring formation. *J. Fluid Mech.* **360**, 121–140.

GREEN, G. 1835 Researches on the vibration of pendulums in fluid media. *Trans. R. Soc. Edinburgh* **13** (1), 54–62.

HEIL, M. 1996 The stability of cylindrical shells conveying viscous flow. *J. Fluids Struct.* **10**, 173–196.

HEIL, M. & JENSEN, O. E. 2003 Flows in deformable tubes and channels: theoretical models and biological applications. In *Flow Past Highly Compliant Boundaries and in Collapsible Tubes*, Fluid Mechanics and Its Applications, Vol. 72, pp. 15–49. Springer.

HO, C.-M. & GUTMARK, E. 1987 Vortex induction and mass entrainment in a small-aspect-ratio elliptic jet. *J. Fluid Mech.* **179**, 383–405.

KECECIOGLU, I., MCCLURKEN, M. E., KAMM, R. D. & SHAPIRO, A. H. 1981 Steady, supercritical flow in collapsible tubes. Part 1. Experimental observations. *J. Fluid Mech.* **109**, 367–389.

KRIEG, M. & MOHSENI, K. 2008 Thrust characterization of a bioinspired vortex ring thruster for locomotion of underwater robots. *IEEE J. Ocean. Engng* **33** (2), 123–132.

KRIEG, M. & MOHSENI, K. 2010 Dynamic modelling and control of biologically inspired vortex ring thrusters for underwater robot locomotion. *IEEE Trans. Robot.* **26** (3), 542–554.

KRIEG, M. & MOHSENI, K. 2013 Modelling circulation, impulse and kinetic energy of starting jets with non-zero radial velocity. *J. Fluid Mech.* **719**, 488–526.

KRUEGER, P. S. 2001 The significance of vortex ring formation and nozzle exit over-pressure to pulsatile jet propulsion. PhD thesis, California Institute of Technology.

KRUEGER, P. S., DABIRI, J. O. & GHARIB, M. 2003 Vortex ring pinchoff in the presence of simultaneously initiated uniform background co-flow. *Phys. Fluids* **15** (7), L49–L52.

KRUEGER, P. S., DABIRI, J. O. & GHARIB, M. 2006 The formation number of vortex rings formed in uniform background co-flow. *J. Fluid Mech.* **556**, 147–166.

KRUEGER, P. S. & GHARIB, M. 2003 The significance of vortex ring formation to the impulse and thrust of a starting jet. *Phys. Fluids* **15** (5), 1271.

KRUEGER, P. S. & GHARIB, M. 2005 Thrust augmentation and vortex ring evolution in a fully-pulsed jet. *AIAA J.* **43** (4), 792–801.

LIEPMANN, D. & GHARIB, M. 1992 The role of streamwise vorticity in the near-field entrainment of round jets. *J. Fluid Mech.* **245**, 643–668.

LOVE, A. E. H. 1944 *A Treatise on the Mathematical Theory of Elasticity*. Dover.

MAXWORTHY, T. 1972 The structure and stability of vortex rings. *J. Fluid Mech.* **51**, 15–32.

MOSLEMI, A. A. 2010 Propulsive efficiency of a biomorphic pulsed-jet underwater vehicle. PhD thesis, Southern Methodist University.

MOSLEMI, A. A. & KRUEGER, P. S. 2010 Propulsive efficiency of a biomorphic pulsed-jet underwater vehicle. *Bioinspir. Biomim.* **5** (3), 036003.

MOSLEMI, A. A. & KRUEGER, P. S. 2011 The effect of Reynolds number on the propulsive efficiency of a biomorphic pulsed-jet underwater vehicle. *Bioinspir. Biomim.* **6** (2), 026001.

MÜLLER, M. O., BERNAL, L. P., MORAN, R. P., WASHABAUGH, P. D., PARVIZ, B. A., CHOU, T.-K. A., ZHANG, C. & NAJAFI, K. 2000*a* Thrust performance of micromachined synthetic jets. In *AIAA Fluids 2000 Conference*.

NICHOLS, J. T. & KRUEGER, P. S. 2012 Effect of vehicle configuration on the performance of a submersible pulsed-jet vehicle at intermediate Reynolds number. *Bioinspir. Biomim.* **7** (3), 036010.

OLCAY, A. B. & KRUEGER, P. S. 2008 Measurement of ambient fluid entrainment during laminar vortex ring formation. *Exp. Fluids* **44**, 235–247.

PALERMO, T. & FLAUD, P. 1987 Etude de l'effondrement à deux et trois lobes de tubes élastiques. *J. Biophys. Bioméch.* **11**, 105–111.

PETRICH, J. 2009 Improved guidance, navigation, and control for autonomous underwater vehicles: theory and experiment. PhD thesis, Virginia Polytechnic Institute and State University.

PETRICH, J., NEU, W. L. & STILWELL, D. J. 2007 Identification of a simplified auv pitch axis model for control design: theory and experiments. In *OCEANS 2007*, pp. 1–7.

PETRICH, J. & STILWELL, D. J. 2010 Model simplification for auv pitch-axis control design. *Ocean Engng* **37** (7), 638–651.

PRANDTL, L. 1952 *Essentials of Fluid Dynamics: With Applications to Hydraulics, Aeronautics, Meteorology and other Subjects*. Hafner.

REYNOLDS, W. C., PAREKH, D. E., JUVET, P. J. D. & LEE, M. J. D. 2003 Bifurcating and blooming jets. *Annu. Rev. Fluid Mech.* **35**, 295–315.

RUIZ, L. A., WHITTLESEY, R. W. & DABIRI, J. O. 2011 Vortex-enhanced propulsion. *J. Fluid Mech.* **668**, 5–32.

SHADDEN, S. C., DABIRI, J. O. & MARSDEN, J. E. 2006 Lagrangian analysis of fluid transport in empirical vortex ring flows. *Phys. Fluids* **18**, 047105.

SHARIFF, K. & LEONARD, A. 1992 Vortex rings. *Annu. Rev. Fluid Mech.* **24**, 235–279.

SIEKMANN, J. 1962 On a pulsating jet from the end of a tube, with application to the propulsion of certain aquatic animals. *J. Fluid Mech.* **15** (03), 399–418.

TRUONG, N. K. & BERTRAM, C. D. 2009 The flow field downstream of a collapsible tube during oscillation onset. *Commun. Numer. Meth. Engng* **25**, 405–428.

WEIHS, D. 1977 Periodic jet propulsion of aquatic creatures. *Forsch. Zool.* **24**, 171–175.